Journal of Materials Chemistry A

ROYAL SOCIETY OF CHEMISTRY

PAPER

View Article Online
View Journal | View Issue

Cite this: J. Mater. Chem. A, 2025, 13, 22583

Silicon/graphite composite host for tuned lithiophilicity in Li metal anodes†

Maryam Tahertalari, Syed Abdul Ahad, Dominika Capkova, Kevin. M. Ryan and Hugh Geaney *

Lithium metal anodes (LMAs) are promising for next-generation high energy density (ED) batteries due to their exceptional theoretical capacity (3860 mAh g^{-1}) and low electrochemical potential (−3.04 V *vs.* the standard hydrogen electrode). However, several issues including lithium (Li) dendrite growth formation, poor coulombic efficiency (CE), and unstable solid electrolyte interphase (SEI) formation hinder their practical performance. Here, we developed a LMA current collector (CC) prepared with a silicon (Si)/graphite (Gr) composite layer on copper (Cu) foil. The lithiophilicity of the CC enabled improved stability during extended Li plating/stripping. In full-cell testing the Li/Cu–Si/Gr anode *versus* sulfur and lithium nickel manganese cobalt oxide (NMC811), delivered average CE values of 95% and 98.82% during 150 charge/discharge cycles at 0.2C, respectively. Rate capability tests revealed that Li/Cu–Si/Gr enabled high areal capacities of 0.837 mAh cm^{-2} *versus* sulfur and 0.607 mAh cm^{-2} *versus* NMC at a high C-rate of 1C. This work highlights the possibility of harnessing conventional Li-ion battery anode materials as surface-modifying lithiophilic agents for LMAs.

Received 28th April 2025
Accepted 6th June 2025

DOI: 10.1039/d5ta03361f

rsc.li/materials-a

1. Introduction

The commercialization of Li-ion batteries (LIBs) has underpinned the development of portable electronics, electric vehicles (EVs), and smart energy grids. However, LIBs are approaching their limits in terms of energy density (ED) and are becoming a bottleneck in applications demanding high ED such as EVs.[1] To address this issue, Li metal anodes (LMAs) are highly promising due to their ideal electrochemical potential (−3.04 V *vs.* the standard hydrogen electrode) and extremely high theoretical capacity (3860 mAh g^{-1}).[2,3] While LIBs typically operate *via* Li^+ intercalation, Li metal batteries (LMBs) function through direct deposition and dissolution of Li^+/Li^0. This approach offers almost 10 times the theoretical specific capacity of commercial Gr anodes (372 mAh g^{-1}).[4] Unfortunately, 'hostless' LMAs typically exhibit poor reversibility upon cycling, caused by uneven/dendritic deposition of Li metal, coupled with large volume expansion and formation of electrically isolated Li (*i.e.*, dead Li). This results in excessive electrolyte consumption, increased cell polarization, accelerated capacity degradation and significant safety concerns such as thermal runaway in the event of short circuit.[5,6] Moreover, due to the highly reducing nature of Li metal, unstable and fragile SEI growth leads to significant loss of active material and low CE.[7,8] These issues cause rapid failure and a shortened lifespan for LMBs, inspiring research into a range of technical solutions.[9] The various strategies adopted to overcome the challenges of LMAs include: (i) electrolyte engineering such as using (localized) high concentrated electrolyte ((L)HCE),[10,11] electrolyte additives[12] and solid-state electrolytes[13] (ii) *in situ* or *ex situ* artificial SEI formation[14,15] and (iii) implementing lithiophilic host structures accommodated to regulate Li deposition.[16–19]

This development of lithiophilic host structures has received considerable attention, with the aim of preparing lightweight hosts for Li that do not significantly dilute the ED of the commercial full cell. ED is a key cell characteristic that is significantly influenced by the current collector used. Some Li hosts are based upon heavy and voluminous foam or 3D structures, which can immediately reduce the ED of the system. In contrast, planar Cu foil is lightweight, low-density and cost-effective and has been widely implemented in LIBs.[20–22] However, Cu's highly lithiophobic nature as well as low specific surface area leads to heterogenous and dendritic Li growth.[23,24] To address this, a range of lithiophilic materials (*e.g.* Cu_2O,[25] ZnO,[26] Ag[27] and Sn[28]) have been incorporating onto planar Cu, to induce lithiophilicity of the CC and regulate Li stripping/plating.

Lithiophobic carbonaceous based materials including porous graphene networks,[29] reduced graphene oxide (rGO),[30] porous carbon films[31] and carbon nanofibers (CNFs)[32] have all been studied as matrices to host Li, due to their high specific surface area (SSA), good ion/electron conductivity, low weight, and ability to accommodate Li without increasing local current

Department of Chemical Sciences and Bernal Institute, University of Limerick, Ireland. E-mail: hugh.geaney@ul.ie

† Electronic supplementary information (ESI) available: CE testing of electrodes, SEM cross-sectional imaging, CE testing of Li–S cells and voltage profiles. See DOI: https://doi.org/10.1039/d5ta03361f

density. However, due to their lithiophobic nature, modifying carbon structures through heteroatom doping, compositing with metal oxides (*e.g.* ZnO,[33] Co_3O_4,[34] V_2O_5,[35] CuO,[36] Al_2O_3,[37] *etc.*), or generating specific electrode architectures can be used to regulate Li nucleation and plating/stripping dynamics.[38]

Beyond these mentioned carbon materials, alternatives such as Gr (the stalwart of LIBs) can also be used as hosts for LMAs. It has been widely demonstrated that after Li ions intercalate into natural Gr anode up to a capacity of 372 mAh g^{-1}, Li metal deposits grow into Li dendrites due to weak Li affinity and limited space. While synthetic Gr with 2D flakes, has scope for additional Li storage in internal edge-plane spaces, at higher current densities (>0.2 C) and capacities (>744 mAh g^{-1}), limited space and poor Li affinity lead to dendritic Li formation.[38] Similar to the other carbon-based hosts, Gr is also considered intrinsically lithiophobic, which results in poor Li_{liq} spreading on a Gr surface[39] (and is linked to problematic Li plating in LIBs). To address this, several strategies have been examined such as expanding Gr (*e.g.*, by heating), increasing the interlayer spacing/surface area to enhance Li accommodation and providing nucleation sites[40] and/or using lithiophilic coatings to induce lithiophilicity.[41] In particular, fabricating composites containing lithiophilic substances, like Li alloying materials (*e.g.* Si, Sn or Ge)[42–45] to improve the lithiophilicity of carbon-based materials including Gr is attractive.

Si is a prominent candidate for Li plating/stripping due to a strong Li affinity, eco-friendliness, earth-abundant, cost-effectiveness, while it is also lighter than most lithiophilic metal oxides.[46] However, pure Si anodes face challenges such as unstable SEI formation due to huge volume change of Si during alloying/dealloying with Li.[47,48] To tackle this obstacle combining Si with Gr has previously been extensively investigated for Li-ion battery (LIB) anodes.[49–51]

Therefore, Gr composites containing lithiophilic Si have potential as a Li affinitive host. Gr can stabilize the SEI by accommodating volume changes of pure Si during early cycles (where SEI formation is dominant). A thin layer of the tuned composite on the Cu CC can improve the lithiophilicity of the planar Cu by limiting the formation of Li dendrites through regulating Li deposition flux, increasing the specific surface area (relative to planar Cu CC) and reducing the local current density of the Cu CC, while accommodating the Li related volume changes during Li plating/stripping cycles.[52,53]

In this study, the influence of Si/Gr composite coatings on Cu CCs as lithiophilic layers for hosted LMAs is examined. The impact of Si content on the reversibility of Li plating/stripping was probed systematically for Cu–$Si_{05}Gr_{95}$, Cu–$Si_{10}Gr_{90}$, Cu–$Si_{15}Gr_{85}$ and Cu–$Si_{20}Gr_{80}$, as well as bare Gr (Cu–$Si_{00}Gr_{100}$), bare Si (Cu–$Si_{100}Gr_{00}$) and bare Cu. Si incorporation into composite enhances the lithiophilicity, leading to homogeneous Li deposition using the optimum composition LMA (Cu–$Si_{10}Gr_{90}$). This LMA demonstrates suppressed dendritic Li compared to the control CC and other compositions, enabling extended cycling with high CEs of 94.8% and 98.1% at capacities of 1 mAh cm^{-2} and 3 mAh cm^{-2} at a current density of 1 mA cm^{-2} *vs.* Li foil, respectively. Moreover, the Cu–$Si_{10}Gr_{90}$ lowers the nucleation overpotentials of bare Cu by 14 times and Gr by 1.7 times. The optimum LMA also outperforms Cu, Cu–$Si_{00}Gr_{100}$ and Cu–$Si_{20}Gr_{80}$ anodes in full-cell assessments by achieving high average CEs of 95% *vs.* sulfur and 97.8% *vs.* NMC cathodes during 150 charge/discharge cycles at 0.2C. Hence, the Cu–$Si_{10}Gr_{90}$ CC shows potential to enhance the commercial use of high ED Li metal-based batteries such as Li–S batteries.

2. Results and discussion

2.1. Li plating/stripping performance of the LMA hosts

To determine the Li plating/stripping performance of various Si/Gr composite coatings, CE tests were conducted by assembling Cu–Si/Gr electrodes against Li foil. The various composite substrates of Si/Gr included Cu–$Si_{00}Gr_{100}$, Cu–$Si_{05}Gr_{95}$, Cu–$Si_{10}Gr_{90}$, Cu–$Si_{15}Gr_{85}$, Cu–$Si_{20}Gr_{80}$, and Cu–$Si_{100}Gr_{00}$, with Cu foil used as a control. Initial cycling included charge/discharge step between 0.01–1 V for 5 cycles (Fig. S12†) for SEI stabilization followed by subsequent Li plating below 0 V and stripping up to 0.2 V only (Fig. 1a). The approach means that the anodes operate using only the plated Li (for reversible stripping and plating), rather than delithiating the Si and Gr component on the CC. The onset of metallic Li plating below 0 V indicates the degree of lithiophilicity of the structures and was measured by determining the nucleation overpotential (Fig. 1b).[24,54] Cu–$Si_{10}Gr_{90}$ showed the highest lithiophilicity, as determined from its lowest nucleation overpotential of 9 mV, which is below that of the Cu–$Si_{20}Gr_{80}$ (10.6 mV). Nucleation overpotential of Cu–$Si_{15}Gr_{85}$ (9.8 mV, Fig. S1e†) stands in between those of 10% and 20% Si. In contrast, the Cu–$Si_{00}Gr_{100}$ CC had a higher nucleation overpotential of 16 mV, which is consistent with its established lithiophobic behaviour.[41] Finally, Cu foil due to its entirely lithiophobic nature and low surface-area which precludes guided Li deposition, had a significantly high nucleation overpotential of 127 mV. Based on the comparison of nucleation overpotential values, it indicates that a limited amount of Si (10%), leads to the most lithiophilic CC among other compositions.

The CE testing performed at 1 mA cm^{-2} current density and 1 mAh cm^{-2} plating capacity, further shed light on the impact of the lithiophilic character on the Li plating/stripping reversibility. The pure Gr coated CC (Cu–$Si_{00}Gr_{100}$) delivered an unstable CE that fluctuated between 70 to 90% during 50 cycles before a rapid drop (Fig. 1c). This can be linked to its lithiophobic nature,[41] which causes unstable Li deposition/stripping and obvious irreversibility in the anode. Pristine Cu foil (Fig. S1a and b†) was found to deliver the least stable CE values of all, with less than 20 cycles sustained, aligning with its lithiophobic nature and extremely high nucleation overpotential, leading to uneven Li deposition.[55] The data for Cu–$Si_{10}Gr_{90}$ (Fig. 1d), shows that a Si content of 10% enabled much more stable Li plating/stripping for more than 120 cycles, with an average CE of 94.8%. This was a marked improvement compared to the 5% Si anode (Fig. S1c†), which dropped from 60 cycles delivering an average CE of 94.6% during 80 cycles suggesting lithiophobicity of Gr in the composition is dominant due to insufficient lithiophilic Si content (only 5%) in the composition confirmed by its higher nucleation overpotential

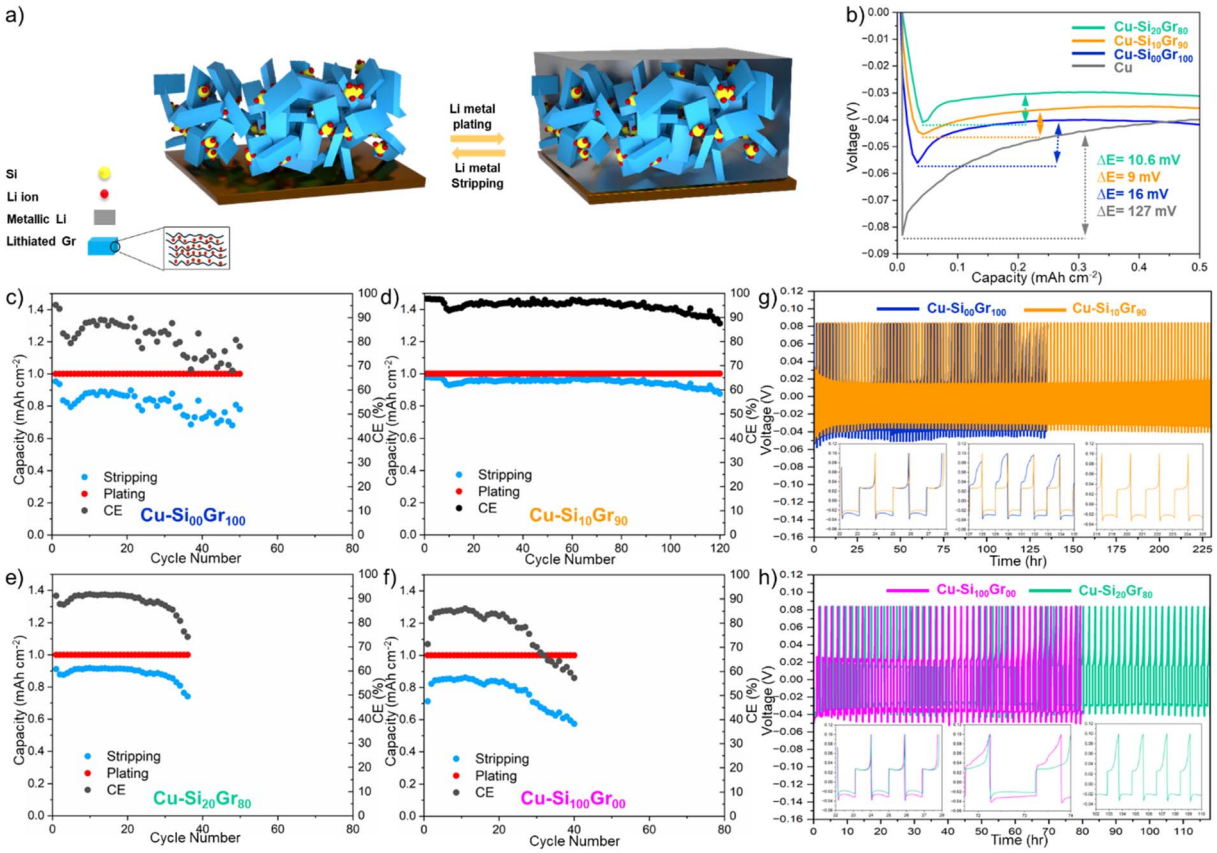

Fig. 1 (a) Schematics of the composite coated substrates before and after plating Li. (b) Nucleation overpotential of Cu–$Si_{10}Gr_{90}$, Cu–$Si_{20}Gr_{80}$, Cu–$Si_{00}Gr_{100}$ and Cu tested at 1 mA cm^{-2}. CE test of (c) Cu–$Si_{00}Gr_{100}$ (d) Cu–$Si_{10}Gr_{90}$ (e) Cu–$Si_{20}Gr_{80}$ and (f) Cu–$Si_{100}Gr_{00}$ at 1 mA cm^{-2} current density and 1 mAh cm^{-2} areal capacity. Corresponding voltage–time plots of (g) Cu–$Si_{00}Gr_{100}$ and Cu–$Si_{10}Gr_{90}$, and (h) Cu–$Si_{20}Gr_{80}$ and Cu–$Si_{100}Gr_{00}$ at different cycle numbers.

(9.8 mV, Fig. S1e†) compared to 10% Si. However, the experiments showed that exceeding 10% Si content in the anode led to a decline in the CE. Cu–$Si_{15}Gr_{85}$ and Cu–$Si_{20}Gr_{80}$ had stable performance for only 50 and 30 cycles, respectively (Fig. S1c† and 1e). Additionally, pure Si CC coating Cu–$Si_{100}Gr_{00}$, had the worst CE among the coated substrates, with an average CE of 77% for only 40 cycles before a rapid decline to much lower values (Fig. 1f). Another important factor influencing the lower Li plating/stripping average CEs of the CCs with higher Si concentration (*i.e.*, Cu–$Si_{20}Gr_{80}$ and Cu–$Si_{100}Gr_{00}$) is electrode degradation caused by unstable SEI as a result of huge volume change of Si[56–59] during initial charge/discharge cycles. As average CEs obtained for Cu–$Si_{15}Gr_{85}$, Cu–$Si_{20}Gr_{80}$ and Cu–$Si_{100}Gr_{00}$ during initial cycling were 89.2%, 84.5% and 75.4%, respectively (Fig. S12f†). Therefore, the 10% Si concentration had the correct balance between the lithiophilic Si and lithiophobic Gr to guide stable Li plating/stripping behaviour.

Stable Li plating/stripping within the Cu–Si_xGr_y CC can be influenced by (1) Gr's high electric conductivity, high SSA and more importantly its ability to accommodate huge volume changes of Si & Li and (2) the capability of Si to create lithiophilic sites, enhancing Si/Gr composite lithiophilicity, which promotes homogeneous Li deposition across the surface.[60–62]

For further examination of the Cu–$Si_{10}Gr_{90}$ CC, plating/stripping cycles were performed for a higher areal capacity of 3 mAh cm^{-2} while maintaining the current density of 1 mA cm^{-2}. The data demonstrates that using even the higher plating areal capacity, the average CE achieved is even slightly higher (98.1%) (Fig. S2a†) than that of plating/stripping at 1 mA cm^{-2} (94.8%) (Fig. 1d). The anode showed stable overpotentials for more than 700 h of plating/stripping (Fig. S2b†), with selected cycles (1, 10, 50, 100 and 120 (Fig. S2c†)) illustrating the stability of Li deposition/dissolution. The voltage–time profiles were also examined to investigate the overpotentials during plating/striping cycles. Cu–$Si_{10}Gr_{90}$ delivers the lowest and steadiest overpotential over the course of 230 h while Cu–$Si_{00}Gr_{100}$ demonstrates highly erratic behaviour in only 135 h time (Fig. 1g). The overpotentials of the Cu–$Si_{100}Gr_{00}$ CC stands higher than that of Cu–$Si_{20}Gr_{80}$ and after 65 h it further increased (Fig. 1h). Cu–$Si_{20}Gr_{80}$ retained stable overpotentials for up to approximately 120 h.

2.2. Morphology assessment of the cycled hosts

The Li plating/stripping behaviours of Cu–$Si_{00}Gr_{100}$, Cu–$Si_{10}Gr_{90}$, Cu–$Si_{20}Gr_{80}$ and Cu–$Si_{100}Gr_{00}$ substrates after 10 plating/stripping cycles for an areal capacity of 1 mAh cm^{-2}

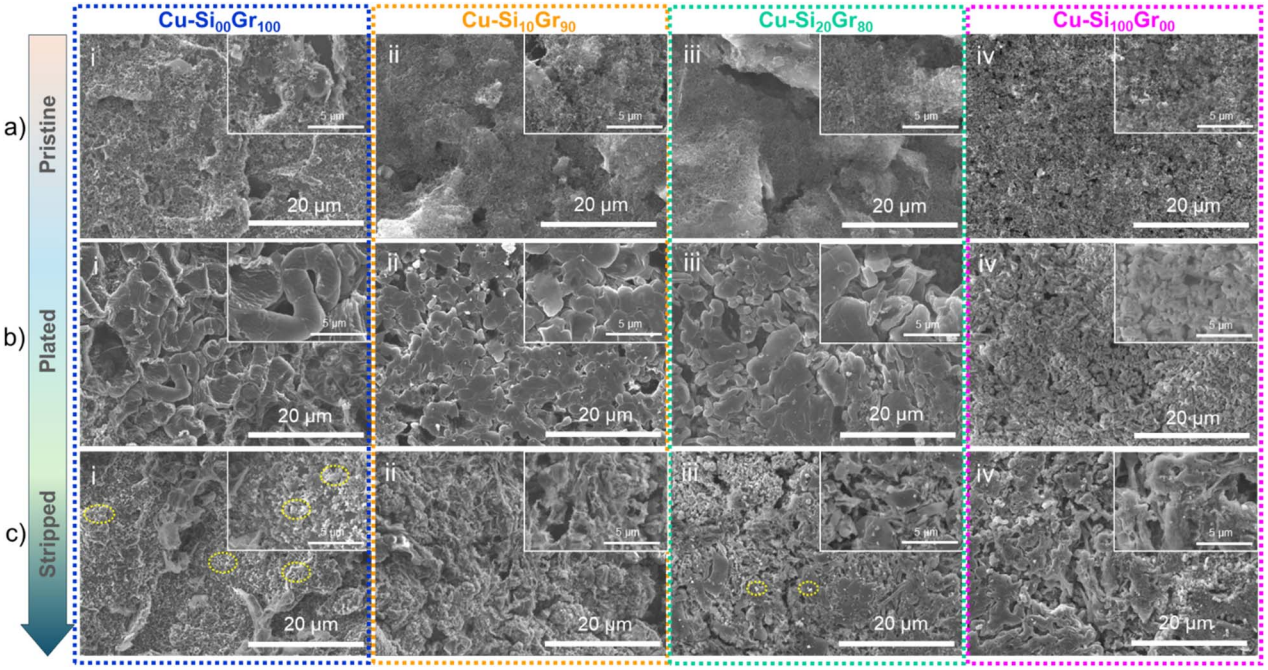

Fig. 2 SEM images of (a) pristine, (b) at the 10th Li plated and, (c) 10th stripped cycle at a current density of 1 mA cm^{-2} and an areal capacity of 1 mAh cm^{-2} for the (i) Cu–$Si_{00}Gr_{100}$, (ii) Cu–$Si_{10}Gr_{90}$, (iii) Cu–$Si_{20}Gr_{80}$ and (iv) Cu–$Si_{100}Gr_{00}$ electrodes with two different magnitudes of 5 and 20 μm.

using 1 mA cm^{-2} current density were visualized using SEM. Images of the pristine substrates (fully lithiated substrates prior to Li plating) are also provided as references (Fig. 2a (i)–(iv)). The Li plating on the Cu–$Si_{00}Gr_{100}$ CC shows Li dendrite formation, with large Li filament size and anisotropic character,[63,64] which emphasizes the lithiophobic behaviour of the CC (Fig. 2b(i)). In contrast, the Li plated on Cu–$Si_{10}Gr_{90}$ is composed of smooth and connected Li islands, showing the impact of incorporating lithiophilic Si on the plated Li morphology (Fig. 2b(ii)). For the Cu–$Si_{20}Gr_{80}$ substrate (Fig. 2b(iii)), a more heterogenous, mixed structure of dendritic Li and Li lumps was seen. Li deposited on Cu–$Si_{100}Gr_{00}$ revealed a porous Li surface (Fig. 2b(iii)), with much smaller Li feature sizes. As the stripped electrodes illustrate, significant Li remnants (denoted by yellow dashes) can be seen for the Cu–$Si_{00}Gr_{100}$ electrode, causing active material loss during plating/stripping cycles and a low CE (Fig. 2c(i)). While no Li dendrite or significant Li remaining was observed for Cu–$Si_{10}Gr_{90}$ (Fig. 2c(ii)) (which aligns with its high CE and low nucleation potential), the Cu–$Si_{20}Gr_{80}$ substrate shows some residual Li on its surface even after being stripped as seen from its low CE (Fig. 2c(iii)). In the case of the Cu–$Si_{100}Gr_{00}$ substrate, its degree of porosity was further increased after the Li was stripped, suggesting that the failure of high Si content CCs is more linked to Si degradation rather than an inability to strip Li (as seen for the Gr containing CCs) (Fig. 2c(iv)).

Dendritic Li was clearly seen on the cross-sectional SEM for Cu–$Si_{00}Gr_{100}$ substrate (Fig. S3a†), with no large-scale dendritic Li visible from the other cross-sections. For Cu–$Si_{00}Gr_{100}$ CC, the plated Li did not penetrate through the entire composite layer, suggesting a top-down plating mechanism.[65,66] EDX analysis of the substrates mapped the increasing Si content, as Cu–$Si_{20}Gr_{80}$ (Fig. S3c†) contains more Si than Cu–$Si_{10}Gr_{90}$ (Fig. S3b†). For Cu–$Si_{10}Gr_{90}$ and Cu–$Si_{20}Gr_{80}$, the plated Li could be seen to permeate throughout the lithiophilic Si/Gr layer. Additionally, it was noted that there was slight detachment of the Cu–$Si_{20}Gr_{80}$ composite from the underlying CC, which is likely again linked to the lithiation induced expansion of the higher Si content (as discussed earlier).[67,68] The Cu–$Si_{100}Gr_{00}$ CC (Fig. S3d†) emphasizes this point as it shows an absence of elemental Cu in the EDX mapping due to the complete detachment of the composite layer from the Cu foil after cycling (Fig. S3d†).[69]

2.3. Full–cell testing *vs.* sulfur and NMC811 cathodes

Sulfur (S) was chosen as a suitable cathode for pairing with the LMAs to validate their practical use in Li–S batteries. Sulfur electrodes with mass loadings of ~1 mg cm^{-2} were paired with Li pre-deposited CCs providing an N/P ratio of 2, as well as employing 1 M LiTFSI in DOL : DME (1 : 1, v/v) + 0.25 M $LiNO_3$ electrolyte. Cyclic performance tests for full-cells of sulfur *vs.* Cu–$Si_{10}Gr_{90}$@Li, Cu–$Si_{20}Gr_{80}$@Li, Cu–$Si_{00}Gr_{100}$@Li and Cu@Li were performed at 0.2C (Fig. 3a). The results revealed that Cu–$Si_{10}Gr_{90}$@Li–S achieved a high initial areal capacity of 1 mAh cm^{-2} compared to the Cu–$Si_{20}Gr_{80}$@Li–S and Cu–$Si_{00}Gr_{100}$@Li–S with ~0.9 mAh cm^{-2} initial capacities. Also, Cu–$Si_{10}Gr_{90}$@Li–S, after 150 cycles, retained a higher discharge areal capacity of ~0.4 mAh cm^{-2} while delivering an average CE of 95% (Fig. 3a) similar to Li–S half cell performance (Fig. S4b†). In contrast, the areal capacity retention for Cu–$Si_{20}Gr_{80}$@Li–S was recorded at

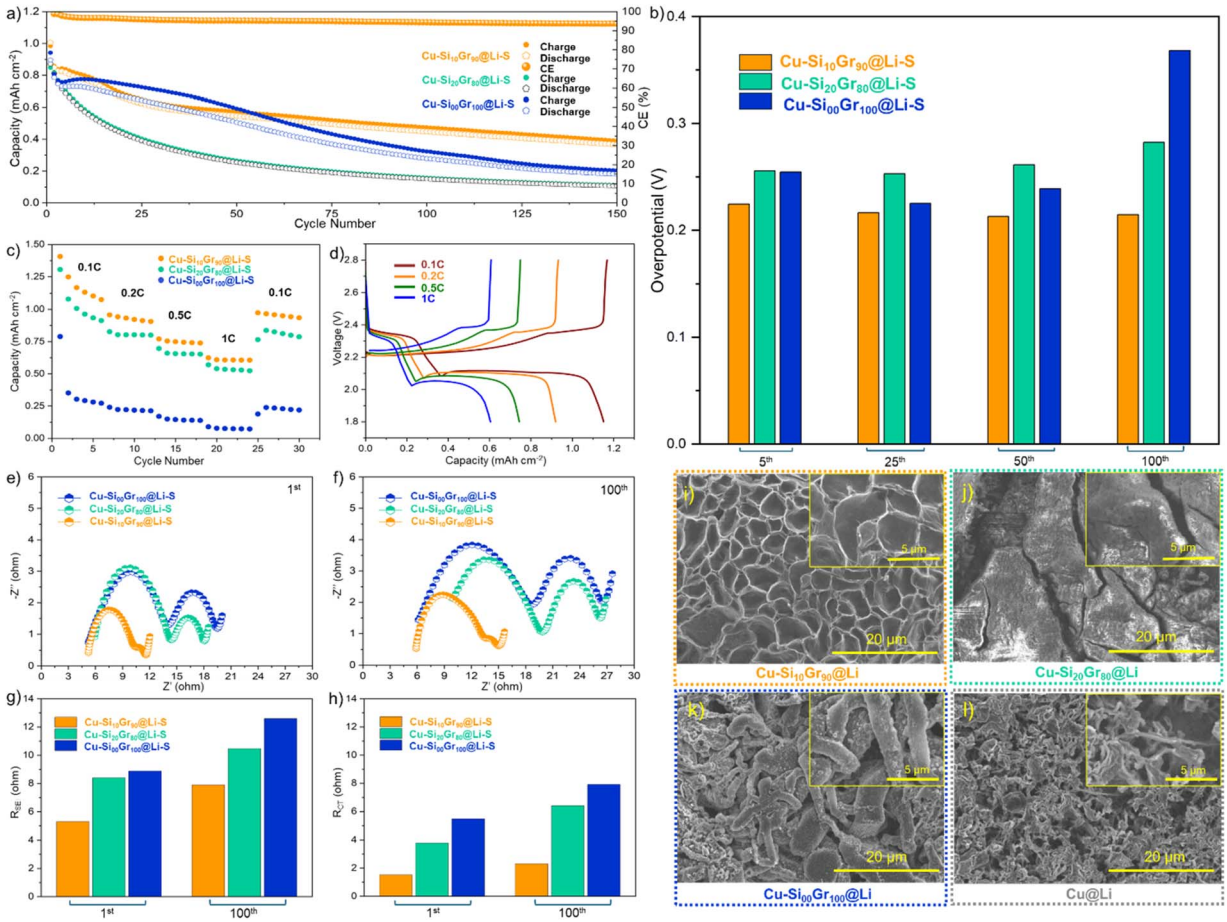

Fig. 3 Cyclic performance of (a) Cu–Si$_{10}$Gr$_{90}$@Li, Cu–Si$_{20}$Gr$_{80}$@Li and Cu–Si$_{00}$Gr$_{100}$@Li in Li–S battery at 0.2C for 150 cycles. (b) Overpotentials for the 5th, 25th, 50th and 100th cycles. (c) Rate capability test of Cu–Si$_{10}$Gr$_{90}$@Li–S, Cu–Si$_{20}$Gr$_{80}$@Li–S and Cu–Si$_{00}$Gr$_{100}$@Li–S at C-rates of 0.1C, 0.2C, 0.5C and 1C, and (d) equivalent voltage–capacity plots of Cu–Si$_{10}$Gr$_{90}$@Li–S for the C-rates. EIS analysis after (e) 1st and (f) 100th cycles and corresponding (g) R_{SEI} and (h) R_{CT} plots for Li–S cells. Post-cycling SEM analysis of the Li–S cells including (i) Cu–Si$_{10}$Gr$_{90}$@Li, (j) Cu–Si$_{20}$Gr$_{80}$@Li, (k) Cu–Si$_{00}$Gr$_{100}$@Li and (l) Cu@Li.

only ~12% with an average CE of 96% (Fig. 3a) and for Cu–Si$_{00}$Gr$_{100}$@Li–S it was 20% with an average CE of 87.7% (Fig. 3a).

The overpotential values were extracted from voltage-capacity graphs (Fig. S5†) for the 5th, 25th, 50th and 100th cycle (Fig. 3d). Cu–Si$_{10}$Gr$_{90}$@Li–S showed lower overpotentials (0.224, 0.216, 0.212 and 0.214 V) compared to Cu–Si$_{00}$Gr$_{100}$@Li–S (0.255, 0.252, 0.261 and 0.282 V) and Cu–Si$_{00}$Gr$_{100}$@Li–S (0.254, 0.225, 0.238 and 0.368 V). As higher overpotential is a sign of heterogeneous Li deposition,[70] the much higher overpotential values for Cu–Si$_{00}$Gr$_{100}$@Li–S once again denotes Li dendrites growth as shown earlier (Fig. 2b). In contrast, lower overpotentials of Cu–Si$_{10}$Gr$_{90}$@Li–S are considered as a factor of homogeneous Li plating as seen for Cu–Si$_{10}$Gr$_{90}$@Li CC (Fig. 2b).

To showcase the cyclic performance of the anodes, Cu–Si$_{10}$Gr$_{90}$@Li–S, Cu–Si$_{20}$Gr$_{80}$@Li–S and Cu–Si$_{00}$Gr$_{100}$@Li–S, at high C-rates, rate capability test was carried out (Fig. 2c). From the results it can be clearly seen that Cu–Si$_{10}$Gr$_{90}$@Li–S has the highest performance with average delivered capacities of 1.189, 0.928, 0.745 and 0.607 mAh cm^{-2} at 0.1, 0.2, 0.5 and 1C, respectively (Fig. 2c). Cu–Si$_{10}$Gr$_{90}$@Li–S delivered slightly lower average capacities than Cu–Si$_{20}$Gr$_{80}$@Li–S at the same C-rates, while Cu–Si$_{00}$Gr$_{100}$@Li–S demonstrated the lowest average capacities of 0.381, 0.222, 0.147 and 0.077 at 0.1, 0.2, 0.5 and 1C (Fig. 2c). Corresponding voltage-specific capacity plots of the 3rd cycles of each C-rates for Cu–Si$_{10}$Gr$_{90}$@Li–S (Fig. 2d), Cu–Si$_{20}$Gr$_{80}$@Li–S (Fig. S6†) and Cu–Si$_{00}$Gr$_{100}$@Li–S (Fig. S6†) are also provided from which increasing overpotentials with respect to the higher C-rates is obvious.

Electrochemical impedance spectroscopy (EIS) results (Fig. 3e and f) indicate that after the 1st cycle, while Cu–Si$_{10}$Gr$_{90}$@Li–S shows much lower values for R_{SEI} with 5.3 and R_{CT} with 1.52 ohm, Cu–Si$_{00}$Gr$_{100}$@Li–S exhibits the highest R_{SEI} and R_{CT} of 8.41 and 3.78 ohm, respectively (Fig. 3g and h). The same trend occurs for the substrates after 100th cycles, with the increased resistances reaching 12.6 (R_{SEI}) and 7.92 ohm (R_{CT}) for Cu–Si$_{00}$Gr$_{100}$@Li–S, which denote significant electrolyte decomposition and an unstable SEI formation which further causes low CE in response to capacity loss as well as high overpotentials.[71,72] In comparison, Cu–Si$_{10}$Gr$_{90}$@Li–S maintained much lower resistance values of 7.9 (R_{SEI}) and 2.3 (R_{CT}) ohm (R_{CT}), which is consistent with more stable SEI formation

and reduced electrolyte decomposition. R_{SEI} and R_{CT} resistance values (summarized in Fig. S7 and Table S1†) for Cu–Si_{20}-Gr_{80}@Li–S stand at 8.41 and 3.78 ohm after the 1st cycle and 10.47 and 6.41 ohm after the 100th cycle which is almost double the resistances of Cu–$Si_{10}Gr_{90}$@Li–S and slightly less than the values for Cu–$Si_{00}Gr_{100}$@Li–S. The lower R_{SEI} and R_{CT} resistances of Cu–$Si_{10}Gr_{90}$@Li–S reflect the higher CE of Cu–$Si_{10}Gr_{90}$ and lower nucleation barrier (9 mV) (Fig. 1d and b).[73]

SEM analysis was carried out for each Li–S cell anodes at their fully charged state post-cycling. The images show interconnected Li lumps covering the Cu–$Si_{10}Gr_{90}$@Li surface signifying uniform Li deposition on the anode (Fig. 3i), consistent with its high electrochemical performance tested in both half and full-cells, measured cell resistances and low overpotentials.

However, the substrate with increased Si content, Cu–Si_{20}-Gr_{80}@Li, exhibited a surface with noticeable fractures (Fig. 3j), explaining its low-capacity retention, high overpotentials and cell resistances.[64,74] There was significantly more variation in the Li morphology when moving from the 10th cycle post-mortem analysis to the 100th cycle for the Cu–$Si_{20}Gr_{80}$@Li compared to the Cu–$Si_{10}Gr_{90}$@Li LMA. In the case of the optimum Cu–$Si_{10}Gr_{90}$@Li LMA composition, it is able to guide Li deposition for a higher number of cycles than the Cu–$Si_{20}Gr_{80}$@Li.

Consistent with the half-cell SEM observations for the Cu–$Si_{00}Gr_{100}$@Li LMA, there was significant Li dendrite formation, which is aligned with its reduced CE in Li–S testing (Fig. 3k) as well as its high overpotentials and increased cell resistances. Finally, SEM images of Cu@Li reveal non uniform, dense and fine Li dendrites (Fig. 3l) as also seen in the literature,[26,27,62] result in the lowest CE for the Cu@Li anode in Li–S testing (Fig. S4a†) among the LMAs tested.

For further assessment of the LMAs, they were cycled in full cells *versus* a high capacity NMC811 cathode. The first five charge/discharge cycles were carried out at 0.1C as initial stabilization period before switching to 0.2C. This switching resulted in slight decrease in the average delivered specific areal capacities. Again, consistent with the CE tests of the symmetric cells and the full-cell *versus* sulfur, the Cu–$Si_{10}Gr_{90}$@Li-NMC outperformed the other three NMC cells. At the first cycle this cell delivered an areal capacity of 1.38 mAh cm^{-2} reaching 0.77 mAh cm^{-2} after 150 cycles with an average CE of 97.8% (Fig. 4a). Similarly, Cu–$Si_{20}Gr_{80}$@Li-NMC achieved fairly comparable initial and ending specific capacities and CE of 1.36 mAh cm^{-2}, 0.73 mAh cm^{-2} and 97.81% (Fig. 4a), respectively. However, its specific capacity was significantly reduced even before 30 cycles and it continued cycling at a rather lower capacity compared to Cu–$Si_{10}Gr_{90}$@Li-NMC. Cu–$Si_{00}Gr_{100}$@Li-NMC delivered a capacity retention of 40% over the course of 150 cycles with a high average CE of 99.67% with huge capacity fluctuations similar to its behaviour in a half cell (Fig. 4a). Finally, Cu@Li-NMC demonstrated the worst performance, starting with an initial capacity of 1.4 mAh cm^{-2}, with a dramatic drop to 0 mAh cm^{-2} before completing even 40 cycles (Fig. S8†). Corresponding voltage-areal capacity graphs for cycles 10, 25, 50, 100 and 150 are presented in ESI (Fig. S9†).

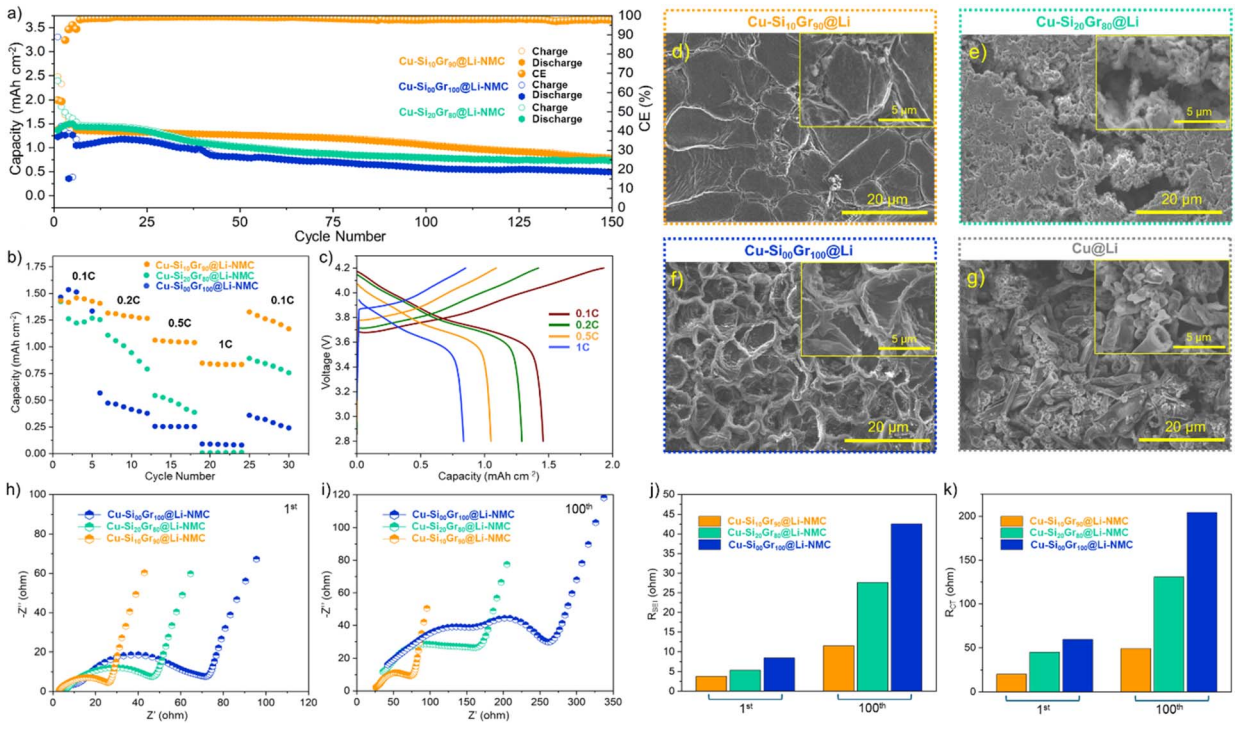

Fig. 4 Cyclic performance of (a) Cu–$Si_{10}Gr_{90}$@Li, Cu–$Si_{20}Gr_{80}$@Li and Cu–$Si_{00}Gr_{100}$@Li substrates *versus* NMC811 cathode at 0.1C for the first five cycles and the remaining 145 cycles at 0.2C. (b) Rate capability test at various C-rates. (c) Voltage-specific areal capacity plots of Cu–$Si_{10}Gr_{90}$@Li-NMC at the various C-rates at the 3rd cycle. Post-cycling SEM analysis of (d) Cu–$Si_{10}Gr_{90}$@Li, (e) Cu–$Si_{20}Gr_{80}$@Li, (f) Cu–$Si_{00}Gr_{100}$@Li and (g) Cu@Li. EIS analysis of full-cells *versus* NMC after the (h) 1st and (i) 100th cycles and corresponding (j) R_{SEI} and (k) R_{CT} plots.

As follow up analysis, rate capability tests of Cu–$Si_{10}Gr_{90}$@Li-NMC, Cu–$Si_{20}Gr_{80}$@Li-NMC and Cu–$Si_{00}Gr_{100}$@Li-NMC were performed at the same C-rates of 0.1, 0.2, 0.5 and 1C (Fig. 4b). Cu–$Si_{10}Gr_{90}$@Li-NMC had superior performance compared to Cu–$Si_{20}Gr_{80}$@Li-NMC and Cu–$Si_{00}Gr_{100}$@Li-NMC delivering 1.43, 1.289, 1.0484 and 0.837 mAh cm^{-2} at 0.1, 0.2, 0.5 and 1C, respectively (Fig. 4b). Cu–$Si_{00}Gr_{100}$@Li-NMC demonstrated the lowest capacities at each C-rates apart from 1C, where it performed slightly better than the Cu–$Si_{20}Gr_{80}$@Li-NMC showing that higher percentages of Si are not compatible with high rate cycling (Fig. 4b). All three Cu–$Si_{10}Gr_{90}$@Li-NMC (Fig. 4c), Cu–$Si_{20}Gr_{80}$@Li-NMC and Cu–$Si_{00}Gr_{100}$@Li-NMC (Fig. S10†) follow the trend of increasing overpotentials with increased C rates.

Post-mortem SEM analysis was carried out for the LMAs taken from the full-cells with NMC. The morphology of Cu–$Si_{10}Gr_{90}$@Li-NMC showed a uniformly plated Li morphology (Fig. 4d), matching the other SEM images of this anode cycled in a full-cell *versus* sulfur and half-cells. The observed porous Li surface with lots of cracks on Cu–$Si_{20}Gr_{80}$@Li explains its plating/stripping efficiency in the cell (Fig. 4e). In contrast, mossy Li structure on Cu–$Si_{00}Gr_{100}$@Li (Fig. 4f) and dendritic Li on Cu@Li (Fig. 4g) signify heterogeneous Li deposition on both, correlating with their poor cycling performances and cell failure.

EIS tests for the three LMAs were conducted (Fig. 4h, i and Table S2†) revealing a trend similar to the EIS results observed in sulfur cells. After the 1st and 100th cycles, the Cu–$Si_{10}Gr_{90}$@Li-NMC had the lowest R_{SEI} (3.8 ohm) and R_{CT} (20.28 ohm) after the 1st cycle and, R_{SEI} (11.5 ohm) and R_{CT} (48.99 ohm) after the 100th cycles (Fig. 4j and k). Cu–$Si_{20}Gr_{80}$@Li-NMC demonstrated increased values for R_{SEI} and R_{CT} resistances of 5.36 and 45.01 ohm after the 1st cycle and, and after the 100th cycles, respectively (Fig. 4j and k). However, the highest resistances belong to Cu–$Si_{00}Gr_{100}$@Li-NMC with R_{SEI} and R_{CT} with 8.5 and 59.5 ohm after only one cycle (Fig. 4j and k). Its resistances further rose to R_{SEI} (42.58 ohm) and R_{CT} (204.58 ohm) after completing 100 cycles (Fig. 4j and k). The lowest resistances of Cu–$Si_{10}Gr_{90}$@Li-NMC even after 100 cycles signifies a reduced electrolyte decomposition and a more stable SEI layer, which helps maintain capacity and improve CE supported by its high half-cell CE and lower nucleation overpotential (9 mV) of Cu–$Si_{10}Gr_{90}$ compared to the other electrodes (Fig. 1b and d).[73] In contrast, higher resistances of Cu–$Si_{00}Gr_{100}$@Li-NMC and the further considerably escalate of the values indicates an unstable SEI formation and severe electrolyte decomposition.[71,72] These factors contribute to a decrease in CE due to capacity loss and elevated overpotentials as was previously highlighted in its low CE and high overpotentials in half cell testing above.[71,72] Additionally, the higher resistance values of Cu–$Si_{10}Gr_{90}$@Li-NMC (R_{SEI}: 11.5 and R_{CT}: 48.99 ohm, Fig. 4i) compared to $Si_{10}Gr_{90}$@Li–S (R_{SEI}: 7.9 and R_{CT}: 2.3 ohm, Fig. 3f) after 100 cycles is due to better compatibility of LMAs with ether-based electrolytes (1 M LiTFSI in DOL : DME (1 : 1, v/v) with 0.25 M $LiNO_3$), used to cycle sulfur cells. These lower R_{SEI} and R_{CT} resistances are as a result of more stable SEI formation compared to NMC cells cycled in a normal carbonate (1 M $LiPF_6$ in EC/DEC with 10% FEC), after 100 cycles.[75,76]

3. Conclusion

This study describes the development of a composite host for LMAs based on Si/Gr, which imparts lithiophilicity to the inherently lithiophobic Cu current collector and thus enables reversible Li plating/stripping for LMAs. The Si/Gr ratio within the composite LMA was systematically examined, with Cu–$Si_{10}Gr_{90}$ providing the lowest nucleation overpotential during Li plating (14 times lower than bare Cu). This lithiophilic character for the optimum Si/Gr composite enabled very high CEs of 94.8% (an areal capacity of 1 mAh cm^{-2} for about 120 cycles) and 98.1% (an areal capacity of 3 mAh cm^{-2} for 110 cycles) in symmetric cells. In practical LMB testing, when the Cu–$Si_{10}Gr_{90}$ LMA was paired with Sulfur or NMC cathode, it again demonstrated the best performance of the various compositions, verifying that a 10% Si content provides the correct degree of lithiophilicity to the Gr matrix for reversible Li plating/stripping. This strategy highlights the key role that Li alloying materials can play within hosted LMAs, to deliver reversible plating/stripping for high ED applications.

4. Experimental section

4.1 Electrode preparation

Si (50 nm nanopowder, 99%, sourced from NanoAmor) were mixed with Gr (~20 μm, synthetic, purchased from Sigma Aldrich) in a mortar and pestle in various ratios to prepare Si/Gr composites namely $Si_{00}Gr_{100}$ (0 wt% Si), $Si_{05}Gr_{95}$ (with 5 wt% Si), $Si_{10}Gr_{90}$ (with 10 wt% Si), $Si_{15}Gr_{85}$ (with 15 wt% Si), $Si_{20}Gr_{80}$ (with 20 wt% Si) and $Si_{100}Gr_{00}$ (100 wt% Si). Electrode slurries were made by combining the active material composites with conductive carbon black (Super C65, sourced from Sigma Aldrich) and carboxymethyl cellulose (CMC, purchased from Sigma Aldrich) binder in 80 : 10 : 10 ratios, respectively. And they were kept stirring for 24 h prior to casting. The slurries then were casted on commercial dendritic Cu foil (Schlenk, 18–20 μm thickness) and dried in a vacuum oven at 80 °C overnight. The composites coated on Cu are denoted as Cu–$Si_{00}Gr_{100}$, Cu–$Si_{05}Gr_{95}$, Cu–$Si_{10}Gr_{90}$, Cu–$Si_{15}Gr_{85}$, Cu–$Si_{20}Gr_{80}$ and Cu–$Si_{100}Gr_{00}$ with loadings of 1–1.2 mg cm^{-2} and coating thickness of ≈40 μm.

4.2. Material characterization

Scanning electron microscopy (SEM) and electron dispersive spectroscopy (EDS) analyses were conducted on a Hitachi SU-70 instrument. The SEM was operated at 5 kV for the analysis of all substrate samples, specifically, for Li-containing samples to avoid sample degradation due to beam damage. For post-mortem analysis of SEM substrate electrodes were extracted from half/full-cells before being washed with dimethoxy ethane (DME) within an Ar-filled glove box. After drying within the glove box, they were transferred into SEM without exposing them to the air.

4.3. Electrochemical measurements

All electrochemical characterizations were performed using CR2032 coin cells assembled in an Ar-filled glove box where O_2

and H_2O levels maintained below 1 ppm. A Neware battery cycler and Biologic (VMP-300) instrument were used for conducting half-cell testing and electrochemical impedance spectroscopy (EIS). For performing CE tests, electrodes including $Cu–Si_{00}Gr_{100}$, $Cu–Si_{05}Gr_{95}$, $Cu–Si_{10}Gr_{90}$, $Cu–Si_{15}Gr_{85}$, $Cu–Si_{20}Gr_{80}$, $Cu–Si_{100}Gr_{00}$ and Cu were assembled against Li foils with the same size as the electrodes, along with using 60 μL of 2.5 M LiTFSI (DOL : DME, 1 : 1, vol%) + 0.25 M $LiNO_3$ electrolyte and Celgard 2325 separator for each cell. The half cells were cycled in a potential window of 0.011–1 V *vs.* Li/Li^+ for five times. After this, Li plating (below zero V) was carried out using a current density of 1 mA cm^{-2} and an areal capacity of 1 mAh cm^{-2} and stripping up to 0.1 V to ensure stripping of all plated Li. For full-cell testing using Sulfur cathodes, ~2.2 mAh cm^{-2} Li (N/P ratio of ~2) was pre-deposited on each substrate and cycled against sulfur cathode at 0.2C between 1.8–2.8 V. For fabricating sulfur electrodes, sulfur, carbon black Super-P, sourced from Thermo Fisher Scientific, >99%) and polyethylene oxide (PEO, purchased from Sigma Aldrich) were casted on a carbon-coated aluminium foil and dried in ambient conditions, before punching out 10 mm diameter electrodes for pairing with the Li pre-electrodeposited substrates. The electrolyte used was 20 μL mg^{-1} of 1 M LiTFSI in DOL : DME (1 : 1) + 0.25 M $LiNO_3$ as well as Celgard 2325 as separator. The NMC811 cathode was procured from NEI Corporation with a high areal capacity of 2 mAh cm^{-2} and nominal mass loading of 10.79 mg cm^{-2}. For assembling full-cells containing NMC811 cathode, 4 mAh cm^{-2} (N/P ratio of 2) Li was pre-deposited on each substrate electrode before being assembled *versus* NMC cathode. For each cell, 60 μL of a carbonate-based electrolyte including 1 M $LiPF_6$ in EC : DEC (1 : 1) + 10% FEC was applied into the full-cells. Because of high operational voltage of NMC cathode (4.3 V) which is beyond ether-based electrolytes oxidation stability (<4 V).[77] The mentioned carbonate-based electrolytes utilized to carry out electrochemical tests of full cells with NMC. The full cells were precycled at 0.1C for five cycles, with the remaining cycles at 0.2C, all within the potential range of 2.8–4.2 V.

Data availability

All data supporting the findings of this study are available within the article and its ESI† files.

Author contributions

M. T.: conceptualization, methodology, materials characterisation, data analysis and curation, visualisation and writing original draft. S. A. A.: methodology, data analysis, writing-review and editing. D. C.: data analysis, review. K. M. R.: supervision, funding acquisition, writing-review and editing. H. G.: methodology, data analysis, writing-review and editing, supervision, funding acquisition. All authors have read and approved the final manuscript.

Conflicts of interest

There are no conflicts to declare.

Acknowledgements

M. T. acknowledges funding from Department of Chemical Sciences and Faculty of Science and Engineering, UL. H. G. acknowledges funding from Science Foundation Ireland Grant 18/SIRG/5484. S. A. A. acknowledges funding from Irish Research Council-GOIPD/2024/208. K. M. R. acknowledges Science Foundation Ireland (SFI) under the Principal Investigator Program under contract no. 16/IA/4629 and under grant no. SFI 16/M-ERA/3419. K. M. R. further acknowledges IRCLA/2017/285 and SFI Research Centers MaREI, AMBER, and CONFIRM 12/RC/2278_P2, 12/RC/2302_P2, and 16/RC/3918. D. C. acknowledges EU Horizon 2023 research and innovation program, Marie Sklodowska-Curie Postdoctoral Fellowship Grant no. 101152715 (SALSA Project).

References

1 R. Schmuch, R. Wagner, G. Hörpel, T. Placke and M. Winter, *Nat. Energy*, 2018, **3**, 267–278.
2 D. Lin, Y. Liu and Y. Cui, *Nat. Nanotechnol.*, 2017, **12**, 194–206.
3 X.-B. Cheng, R. Zhang, C.-Z. Zhao and Q. Zhang, *Chem. Rev.*, 2017, **117**, 10403–10473.
4 X. Chen, X. Liu, X. Shen and Q. Zhang, *Angew. Chem.*, 2021, **133**, 24558–24570.
5 W. Xu, J. Wang, F. Ding, X. Chen, E. Nasybulin, Y. Zhang and J.-G. Zhang, *Energy Environ. Sci.*, 2014, **7**, 513–537.
6 J.-F. Ding, R. Xu, C. Yan, B.-Q. Li, H. Yuan and J.-Q. Huang, *J. Energy Chem.*, 2021, **59**, 306–319.
7 J. F. Ding, R. Xu, X. X. Ma, Y. Xiao, Y. X. Yao, C. Yan and J. Q. Huang, *Angew. Chem.*, 2022, **134**, e202115602.
8 B. Liu, J.-G. Zhang and W. Xu, *Joule*, 2018, **2**, 833–845.
9 F. N. Jiang, S. J. Yang, H. Liu, X. B. Cheng, L. Liu, R. Xiang, Q. Zhang, S. Kaskel and J. Q. Huang, *SusMat*, 2021, **1**, 506–536.
10 J. Zheng, S. Chen, W. Zhao, J. Song, M. H. Engelhard and J.-G. Zhang, *ACS Energy Lett.*, 2018, **3**, 315–321.
11 B. D. Adams, E. V. Carino, J. G. Connell, K. S. Han, R. Cao, J. Chen, J. Zheng, Q. Li, K. T. Mueller and W. A. Henderson, *Nano Energy*, 2017, **40**, 607–617.
12 J. Guo, Z. Wen, M. Wu, J. Jin and Y. Liu, *Electrochem. Commun.*, 2015, **51**, 59–63.
13 Y. Wang, W. D. Richards, S. P. Ong, L. J. Miara, J. C. Kim, Y. Mo and G. Ceder, *Nat. Mater.*, 2015, **14**, 1026–1031.
14 R. Pathak, K. Chen, A. Gurung, K. M. Reza, B. Bahrami, F. Wu, A. Chaudhary, N. Ghimire, B. Zhou and W. H. Zhang, *Adv. Energy Mater.*, 2019, **9**, 1901486.
15 R. Wang, W. Cui, F. Chu and F. Wu, *J. Energy Chem.*, 2020, **48**, 145–159.
16 C.-P. Yang, Y.-X. Yin, S.-F. Zhang, N.-W. Li and Y.-G. Guo, *Nat. Commun.*, 2015, **6**, 8058.
17 C. Jin, O. Sheng, J. Luo, H. Yuan, C. Fang, W. Zhang, H. Huang, Y. Gan, Y. Xia and C. Liang, *Nano Energy*, 2017, **37**, 177–186.

18 K. Chen, R. Pathak, A. Gurung, K. M. Reza, N. Ghimire, J. Pokharel, A. Baniya, W. He, J. J. Wu and Q. Q. Qiao, *J. Mater. Chem. A*, 2020, **8**, 1911–1919.
19 Z. Cao, B. Li and S. Yang, *Adv. Mater.*, 2019, **31**, 1901310.
20 P. Zhu, D. Gastol, J. Marshall, R. Sommerville, V. Goodship and E. Kendrick, *J. Power Sources*, 2021, **485**, 229321.
21 H. Li, L. Wang, Y. Song, Z. Zhang, H. Zhang, A. Du and X. He, *Adv. Funct. Mater.*, 2023, **33**, 2305515.
22 M. Yamada, T. Watanabe, T. Gunji, J. Wu and F. Matsumoto, *Electrochem*, 2020, **1**, 124–159.
23 B. Zhou, A. Bonakdarpour, I. Stoševski, B. Fang and D. P. Wilkinson, *Prog. Mater. Sci.*, 2022, **130**, 100996.
24 K. Yan, Z. Lu, H.-W. Lee, F. Xiong, P.-C. Hsu, Y. Li, J. Zhao, S. Chu and Y. Cui, *Nat. Energy*, 2016, **1**, 1–8.
25 M. Chen, L. Cheng, J. Chen, Y. Zhou, J. Liang, S. Dong, M. Chen, X. Wang and H. Wang, *ACS Appl. Mater. Interfaces*, 2019, **12**, 3681–3687.
26 G. Wang, X. Xiong, P. Zou, X. Fu, Z. Lin, Y. Li, Y. Liu, C. Yang and M. Liu, *Chem. Eng. J.*, 2019, **378**, 122243.
27 S. Cui, P. Zhai, W. Yang, Y. Wei, J. Xiao, L. Deng and Y. Gong, *Small*, 2020, **16**, 1905620.
28 R. Guan, S. Liu, C. Wang, Y. Yang, D. Lu and X. Bian, *Chem. Eng. J.*, 2021, **425**, 130177.
29 R. Mukherjee, A. V. Thomas, D. Datta, E. Singh, J. Li, O. Eksik, V. B. Shenoy and N. Koratkar, *Nat. Commun.*, 2014, **5**, 3710.
30 D. Lin, Y. Liu, Z. Liang, H.-W. Lee, J. Sun, H. Wang, K. Yan, J. Xie and Y. Cui, *Nat. Nanotechnol.*, 2016, **11**, 626–632.
31 S. Huang, L. Tang, H. S. Najafabadi, S. Chen and Z. Ren, *Nano Energy*, 2017, **38**, 504–509.
32 S. Wang, J. Zhang, L. Zhang, X. Hu, X. Qin, X. Yan, Z. Wang, X. Lu, Y. Xin and F. Kang, *Nano Energy*, 2024, **131**, 110255.
33 J. Zhu, H. Zhang, F. Liu and J. Chen, *Ionics*, 2020, **26**, 4381–4390.
34 G. Jiang, N. Jiang, N. Zheng, X. Chen, J. Mao, G. Ding, Y. Li, F. Sun and Y. Li, *Energy Storage Mater.*, 2019, **23**, 181–189.
35 G. Huang, P. Guo, J. Wang, S. Chen, J. Liang, R. Tao, S. Tang, X. Zhang, S. Cheng and Y.-C. Cao, *Chem. Eng. J.*, 2020, **384**, 123313.
36 K. Huang, Z. Li, Q. Xu, H. Liu, H. Li and Y. Wang, *Adv. Energy Mater.*, 2019, **9**, 1900853.
37 L. Fan, S. Li, L. Liu, W. Zhang, L. Gao, Y. Fu, F. Chen, J. Li, H. L. Zhuang and Y. Lu, *Adv. Energy Mater.*, 2018, **8**, 1802350.
38 X. Yan, L. Lin, Q. Chen, Q. Xie, B. Qu, L. Wang and D. L. Peng, *Carbon Energy*, 2021, **3**, 303–329.
39 C. Niu, H. Pan, W. Xu, J. Xiao, J.-G. Zhang, L. Luo, C. Wang, D. Mei, J. Meng and X. Wang, *Nat. Nanotechnol.*, 2019, **14**, 594–601.
40 Q. Zhao, X. Hao, S. Su, J. Ma, Y. Hu, Y. Liu, F. Kang and Y.-B. He, *J. Mater. Chem. A*, 2019, **7**, 15871–15879.
41 J. Duan, Y. Zheng, W. Luo, W. Wu, T. Wang, Y. Xie, S. Li, J. Li and Y. Huang, *Natl. Sci. Rev.*, 2020, **7**, 1208–1217.
42 X.-M. Pham, S. A. Ahad, N. N. Patil, H. Geaney, S. Singh and K. M. Ryan, *Nanoscale Horiz.*, 2024, **9**, 637–645.
43 G. Li, Z. Han, Y. Tan, Q. Wei, E. Mao, J. Du and L. Fu, *Electrochim. Acta*, 2024, **473**, 143504.
44 S. A. Ahad, J. Drews, T. Danner, A. Latz and H. Geaney, *J. Mater. Chem. A*, 2024, **12**, 12250–12261.
45 S. Abdul Ahad, S. Bhattacharya, S. Kilian, M. Ottaviani, K. M. Ryan, T. Kennedy, D. Thompson and H. Geaney, *Small*, 2023, **19**, 2205142.
46 N. Greenwood and A. Earnshaw, *Chemistry of the Elements*, Butterworth-Heinemann, Oxford, UK, 2nd edn, 1997, pp. 328–367.
47 M. Ko, S. Chae and J. Cho, *ChemElectroChem*, 2015, **2**, 1645–1651.
48 A. L. Michan, G. Divitini, A. J. Pell, M. Leskes, C. Ducati and C. P. Grey, *J. Am. Chem. Soc.*, 2016, **138**, 7918–7931.
49 P. Li, J.-Y. Hwang and Y.-K. Sun, *ACS Nano*, 2019, **13**, 2624–2633.
50 M. Yoshio, T. Tsumura and N. Dimov, *J. Power Sources*, 2006, **163**, 215–218.
51 C.-H. Yim, F. M. Courtel and Y. Abu-Lebdeh, *J. Mater. Chem. A*, 2013, **1**, 8234–8243.
52 S. Luo and K. Pei, Construction and Modification of Copper Current Collectors for Improved Li Metal Batteries, *Lithium Batteries-Recent Advances and Emerging Topics*, IntechOpen, 2022.
53 H. Ye, Y. Zhang, Y.-X. Yin, F.-F. Cao and Y.-G. Guo, *ACS Cent. Sci.*, 2020, **6**, 661–671.
54 P. Biswal, S. Stalin, A. Kludze, S. Choudhury and L. A. Archer, *Nano Lett.*, 2019, **19**, 8191–8200.
55 Z. Huang, C. Zhang, W. Lv, G. Zhou, Y. Zhang, Y. Deng, H. Wu, F. Kang and Q.-H. Yang, *J. Mater. Chem. A*, 2019, **7**, 727–732.
56 M. Kim, S. P. Harvey, Z. Huey, S.-D. Han, C.-S. Jiang, S.-B. Son, Z. Yang and I. Bloom, *Energy Storage Mater.*, 2023, **55**, 436–444.
57 M. Nie, D. P. Abraham, Y. Chen, A. Bose and B. L. Lucht, *J. Phys. Chem. C*, 2013, **117**, 13403–13412.
58 J. Zheng, H. Zheng, R. Wang, L. Ben, W. Lu, L. Chen, L. Chen and H. Li, *Phys. Chem. Chem. Phys.*, 2014, **16**, 13229–13238.
59 H. Gu, Q. Lei, Y. Liu, W. Chen, Z.-J. Jiang, X. Chen, J. Wu, J. Ye and Z. Jiang, *Carbon*, 2025, **238**, 120240.
60 P. R. Abel, A. M. Chockla, Y.-M. Lin, V. C. Holmberg, J. T. Harris, B. A. Korgel, A. Heller and C. B. Mullins, *ACS Nano*, 2013, **7**, 2249–2257.
61 L.-L. Lu, J. Ge, J.-N. Yang, S.-M. Chen, H.-B. Yao, F. Zhou and S.-H. Yu, *Nano Lett.*, 2016, **16**, 4431–4437.
62 S. Abdul Ahad, T. E. Adegoke, K. M. Ryan and H. Geaney, *Small*, 2023, **19**, 2207902.
63 Q. Dong, B. Hong, X. Huang, M. Bai and Y. Lai, *Electrochim. Acta*, 2022, **403**, 139646.
64 P. Zou, Y. Sui, H. Zhan, C. Wang, H. L. Xin, H.-M. Cheng, F. Kang and C. Yang, *Chem. Rev.*, 2021, **121**, 5986–6056.
65 N.-L. Shen, H. Liu, W.-B. Tang, Z. Liu, T. Wang, Y. Ma, Y. Zhong, J. He, Z. Zhu and Y. Wu, *Ind. Eng. Chem. Res.*, 2023, **62**, 15360–15377.
66 X. Wang, Z. Chen, K. Jiang, M. Chen and S. Passerini, *Adv. Energy Mater.*, 2024, **14**, 2304229.
67 A. Ghamlouche, M. Müller, F. Jeschull and J. Maibach, *J. Electrochem. Soc.*, 2022, **169**, 020541.

68 M. P. Bonkile, Y. Jiang, N. Kirkaldy, V. Sulzer, R. Timms, H. Wang, G. Offer and B. Wu, *J. Power Sources*, 2024, **606**, 234256.
69 R. Kataoka, Y. Oda, R. Inoue, M. Kitta and T. Kiyobayashi, *J. Power Sources*, 2016, **301**, 355–361.
70 L. Que and W. Chen, *J. Power Sources*, 2023, **557**, 232536.
71 K. Yan, H.-W. Lee, T. Gao, G. Zheng, H. Yao, H. Wang, Z. Lu, Y. Zhou, Z. Liang and Z. Liu, *Nano Lett.*, 2014, **14**, 6016–6022.
72 Y. Zhang, B. Liu, E. Hitz, W. Luo, Y. Yao, Y. Li, J. Dai, C. Chen, Y. Wang and C. Yang, *Nano Res.*, 2017, **10**, 1356–1365.
73 S. M. Boroujeni, A. Fill, A. Ridder and K. P. Birke, *Batteries*, 2021, **7**, 67.
74 L. Gireaud, S. Grugeon, S. Laruelle, B. Yrieix and J.-M. Tarascon, *Electrochem. Commun.*, 2006, **8**, 1639–1649.
75 J. Liu, S. Ihuaenyi, R. Kuphal, J. Salinas, L. Xie, L. Yang, U. Janakiraman, M. E. Fortier and C. Fang, *J. Electrochem. Soc.*, 2023, **170**, 010535.
76 L. Gan, R. Chen, X. Xu, M. Zan, Q. Li, Q. Wang, X. Yu and H. Li, *J. Power Sources*, 2022, **551**, 232182.
77 D. Das, S. Manna and S. Puravankara, *Batteries*, 2023, **9**, 193.